Cr and Ni Doping of $Li_4Ti_5O_{12}$: Cation Distribution and Functional Properties

Doretta Capsoni,[†] Marcella Bini,[†] Vincenzo Massarotti,*[,†] Piercarlo Mustarelli,[†] Stefania Ferrari,[†] Gaetano Chiodelli,[‡] Maria Cristina Mozzati,[§] and Pietro Galinetto[§]

Department of Physical Chemistry "M. Rolla", University of Pavia, viale Taramelli 16, 27100 Pavia, Italy, CNR−IENI, Department of Pavia, viale Taramelli 16, 27100 Pavia, Italy, and CNISM, Department of Physics "A. Volta", University of Pavia, via Bassi 6, 27100 Pavia, Italy

Received: July 21, 2009; Revised Manuscript Received: September 30, 2009

Cr- and Ni-doped $Li_4Ti_5O_{12}$ compound has been characterized through the combined use of X-ray powder diffraction, electron paramagnetic resonance (EPR), ^{7}Li nuclear magnetic resonance magic-angle spinning (NMR-MAS), micro-Raman, and magnetization measurements. The doping, occurring on the octahedral site of the cubic $Li_4Ti_5O_{12}$ spinel lattice, strongly affects both the local and the average structural properties. The glassy character of the observed EPR signals suggests structural disorder in the stable $Li_4Ti_5O_{12}$ matrix and the presence of clustering phenomena or nonhomogeneous distribution of the dopant ion, as also supported by ^{7}Li NMR-MAS, micro-Raman, and magnetization results. The computation by numerical method of the complex EPR signal of the Cr-doped sample suggests that both Cr_{Ti} and Cr_{Li} substitutions occur, giving rise to two distinct EPR components, corresponding to opposite axial distortion of the relative octahedral environments. On the basis of the compositional data, defect models involving oxygen or cation vacancies are proposed to explain the conductivity of the doped material.

1. Introduction

The lithium ion batteries are nowadays widely employed as the main power source for portable electronic devices. Among the studied electrode materials,[1,2] $Li_4Ti_5O_{12}$ (also reported as $Li_{1.33}Ti_{1.67}O_4$) has been intensively investigated for its excellent cycling performances and the reversibility of the lithium insertion/extraction process. The Li^+ ion's migration from the 8a tetrahedral sites to the octahedral 16c empty sites of the cubic spinel structure (*Fd*3*m* S.G.) occurs with small changes in the lattice parameters during the cell cycling.[3,4] However, the very low electronic conductivity[5] of $Li_4Ti_5O_{12}$ represents the limiting factor for a wider application in electrochemical cells and many efforts have been made to overcome this problem by preparing nanocrystals,[6−10] thin films,[11] or by cation doping.[5,12−23] Concerning the last point, different transition metal ions[13−19,23] or divalent and trivalent nontransition ones[5,20−22] have been considered as possible dopants. In the case of Ni and Cr doping, both theoretical[24] and experimental[12,13,18,19] investigations have been carried out, mainly addressed to the electrochemical performances of these materials. However, a detailed analysis of the magnetic and structural local order related to the dopant cation distribution and its influence on the functional properties of these doped compounds, at our knowledge, is still lacking. The Mn substitution has instead been recently investigated, and the dopant distribution on the cationic sites and its valence state have been extensively discussed.[23]

In the present work we report on the study performed on Cr- and Ni-doped $Li_4Ti_5O_{12}$ compound. A careful investigation has been carried out to give new insights into the local and average structural properties, the cations valence states and distribution, the related magnetic response, and the doping effect on the conductivity of the material. This purpose is reached through the combined use of X-ray powder diffraction (XRPD) with structural refinement, electron paramagnetic resonance (EPR), micro-Raman and solid state ^{7}Li nuclear magnetic resonance (NMR) spectroscopies, and magnetic measurements. The conductivity behavior of undoped and doped samples is investigated by means of impedance spectroscopy (IS) measurements. Finally, both structural and functional properties of the Cr- and Ni-doped samples are discussed in comparison to those of the Mn-doped $Li_4Ti_5O_{12}$, for which a completion of the results previously discussed[23] is given by micro-Raman and magnetization investigation.

2. Experimental Methods

The Ni- and Cr-doped powder samples were prepared by treating in air at 1073 K for 60 h a mixture of TiO_2 (Merck, >99%), Li_2CO_3 (Aldrich, 99.6%), NiO (Aldrich, 99.99%), and Cr_2O_3 (Aldrich, 99.995%) in proper amount, to form $Li_{1.317}Ni_{0.050}Ti_{1.633}O_4$ (Ni050 sample) and $Li_{1.317}Cr_{0.050}Ti_{1.633}O_4$ (Cr050 sample), respectively; the formulas are balanced on the basis of a +3 oxidation state for Ni and Cr ions.

The undoped $Li_4Ti_5O_{12}$ and the Mn-doped samples are those previously prepared;[23] in particular, for Mn doping, the synthesis stoichiometry leads to the formulas $Li_{1.333}Mn_{0.050}Ti_{1.616}O_4$ (Mn050 sample; 3C in ref 23) and $Li_{1.333}Mn_{0.167}Ti_{1.500}O_4$ (Mn167 sample; 10C in ref 23).

Room-temperature (r.t.) XRPD measurements were performed in air on a Bruker D5005 diffractometer with the Cu Kα radiation, Ni filter, and a position-sensitive detector (PSD). Rietveld structural and profile refinement was carried out by means of TOPAS V3.0 software.[25]

EPR measurements were performed at about 9.4 GHz with a Bruker spectrometer equipped with a continuous nitrogen flow cryostat to study the temperature dependence from 150 up to 420 K and with an Oxford cryostat with helium continuous flux for the range of 4−150 K. Particular care was paid in

* To whom correspondence should be addressed. Phone: 39-382-987203. Fax: 39-382-987575. E-mail: vincenzo.massarotti@unipv.it.
[†] Department of Physical Chemistry "M. Rolla", University of Pavia.
[‡] CNR−IENI, Department of Pavia.
[§] Department of Physics "A. Volta", University of Pavia.

10.1021/jp906894v CCC: $40.75
Published on Web 10/16/2009

TABLE 1: Lattice Parameters, Isotropic Thermal Factors, Tetrahedron and Octahedron Bond Lengths, Impurities Weight Percentage, Recalculated Stoichiometry, Cation Distribution on the Cationic Framework, and Discrepancy Factors Obtained by Rietveld Structural Refinement

sample	undoped	Cr050	Ni050	Mn050	Mn167
a/Å	8.3573(1)[a]	8.3548(1)	8.3574(1)	8.3540(1)[a]	8.3523(1)[a]
B(tetr)/Å^2	2.4(4)[a]	2.5(3)	2.9(3)	2.9(4)[a]	2.6(4)[a]
tetr-O/Å	1.987(2)	1.976(2)	1.991(2)	1.991(2)	1.985(2)
oct-O/Å	1.992(1)	1.997(1)	1.991(1)	1.989(1)	1.991(1)
% TiO_2			0.5(1)	0.3(7)[a]	
% Li_2TiO_3			4.2(2)	2.0(1)[a]	5.9(2)[a]
calcd stoichiometry	$Li_{1.333}$	$Li_{1.317}$	$Li_{1.279}$	$Li_{1.333}$	$Li_{1.276}$
		$Cr_{0.050}$	$Ni_{0.053}$	$Mn_{0.051}$	$Mn_{0.181}$
	$Ti_{1.667}$	$Ti_{1.633}$	$Ti_{1.668}$	$Ti_{1.616}$	$Ti_{1.543}$[a]
tetr. occup.	Li_1	Li_1	Li_1	$Li_{0.985(4)}$ $Mn_{0.015(4)}$	$Li_{0.963(4)}$ $Mn_{0.037(4)}$[a]
oct. occup.	$Li_{0.333}$	$Li_{0.317}$	$Li_{0.279}$	$Li_{0.348(4)}$	$Li_{0.313(4)}$
		$Cr_{0.050}$	$Ni_{0.053}$	$Mn_{0.036(4)}$	$Mn_{0.144(4)}$
	$Ti_{1.667}$	$Ti_{1.633}$	$Ti_{1.668}$	$Ti_{1.616}$	$Ti_{1.543}$[a]
R_{wp}	7.83[a]	7.81	6.82	7.21[a]	5.81[a]
GOF	1.34[a]	1.34	1.25	1.26[a]	1.20[a]

[a] Data also given in ref 23, and reported for comparison.

determining the sample mass and position in the resonant cavity to compare signal intensities (areas) with those of suitable standards and to estimate the relative amount of the paramagnetic species in the samples. The derivative signal areas were computed by double integration with numerical methods.

A SQUID magnetometer has been used for static magnetization (*M*) measurements in the *T* range of 2−352 K and for magnetic fields ranging between 0 and 3 T.

Micro-Raman and photoluminescence measurements were carried out at r.t. by using a Labram Dilor spectrometer equipped with an Olympus microscope HS BX40. The 488 nm light from Ti:Sapphire laser was employed as excitation radiation and focused on the samples by means of a 100× objective, leading to a laser spot of ∼1 μm of diameter. The spectral resolution was about 1 cm^{-1} mainly due to the usage of a cooled CCD camera with 1024 × 256 pixels. For each sample the spectra were taken from different regions using the micrometer laser spot in order to verify the sample homogeneity degree.

The ^{7}Li NMR measurements were performed at r.t. and 155.6 MHz on a AMX400WB spectrometer (Bruker) based on a 9.4 T magnet. Magic-angle spinning (MAS) spectra were acquired with a 4 mm probe head (Bruker), equipped with cylindrical zirconia rotors and a boron nitride stator. The samples were spun from 5 to 12 kHz, and the data were averaged over 64 acquisitions using a single-pulse sequence, with a 90° pulse of 3 μs and a recycle time of 10 s. The spectra were referenced to an external sample of 1.0 M LiCl in H_2O.

The IS measurements were performed by means of a frequency response analyzer (FRA) Solartron 1260 apparatus in the frequency range of 10^{-3}−10^7 Hz, with the experimental setting described elsewhere.[26] Conductivity measurements were carried out as a function of temperature on disk-shaped samples sintered at 1073 K for 12 h, sputtered with Pt to deposit the electrodes, and inserted in a polythermal electrochemical cell supplied by a guard circuit to minimize the noise. The measurements were performed in gas flow (O_2, N_2) up to 1073 K, after a pellet pretreatment at 1073 K for 6 h in O_2, followed by cooling (5 K/min) down to r.t.

3. Results

3.1. XRPD. The XRPD patterns of the samples can be explained on the basis of the $Li_4Ti_5O_{12}$ reflections (JCPDS card no. 49-0207). In some cases, additional weak peaks pertinent to TiO_2 (rutile) and/or Li_2TiO_3 impurity phases are observed.

All the XRPD patterns were refined starting from the spinel structural model, by applying the Rietveld method. The reliability of the refined parameters is suggested by the satisfactory values of discrepancy factors and goodness of fit, reported in Table 1, as well as the main structural and compositional parameters. The lattice parameters generally decrease after doping, except for Ni050, whose cell parameters remain practically unchanged. The tetrahedra and octahedra bond distances are negligibly influenced by Ni doping, whereas the Cr substitution induces noticeable changes with respect to the undoped $Li_4Ti_5O_{12}$. Reliable refined isotropic thermal factors (*B*) for oxygen and for ions on the octahedral sites are obtained (not reported in the table for sake of simplicity). The *B* factor of the ions on the tetrahedral site is comparable for all the samples; its value, strongly affected by the possible presence of doping ions substituting Li ones, can give indication of the cation distribution on this site. The impurity phases observed in Ni- and Mn-doped samples have been quantified, and their amount is reported in Table 1. From impurity phases weight percentage and synthesis stoichiometry, the lithium, titanium, and dopant amount really present in the spinel phase are estimated by mass balance and reported in Table 1. Starting from this calculated stoichiometry, the doping cation distribution on the two cationic sites is refined. For Ni- and Cr-doped samples the structural refinement leads to satisfactory results indicating that the dopant cation occupies the octahedral site. In fact, by allowing the Cr and Ni doping ions to distribute on both tetrahedral and octahedral sites under suitable restraints (i) a very low amount of dopant is found on the tetrahedra (well below the standard deviation); (ii) a relevant increase of the *B* thermal factor ($B \sim 4$ Å^2) on the tetrahedral site is observed if dopant ions are forced into that site.

For what concerns the Mn doping, it was previously demonstrated[23] that reliable refined results are obtained if the Mn ions may distribute on both octahedral and tetrahedral sites. The cation distribution of Mn050 and Mn167 samples is also given for comparison in Table 1.

3.2. EPR. The r.t. EPR spectra of all the samples are reported in Figure 1. No EPR signal is observed in the undoped sample, as expected. The Cr050 spectrum is composed by the superposition of two main signals, with $g_{eff} \sim 3.7$ and $g_{eff} \sim 2$ (<2), and by other components with lower intensity centered at about 1140 and 4000 G. With increasing the temperature, the g_{eff} values remain unchanged and the intensities decrease, as usually occurs

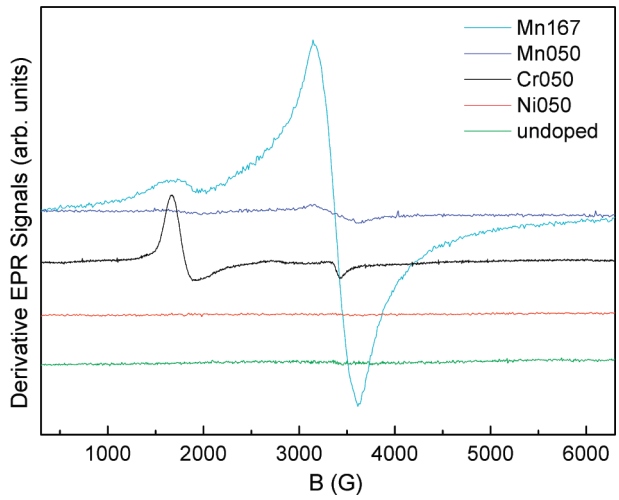

Figure 1. Room-temperature EPR spectra of all the considered samples.

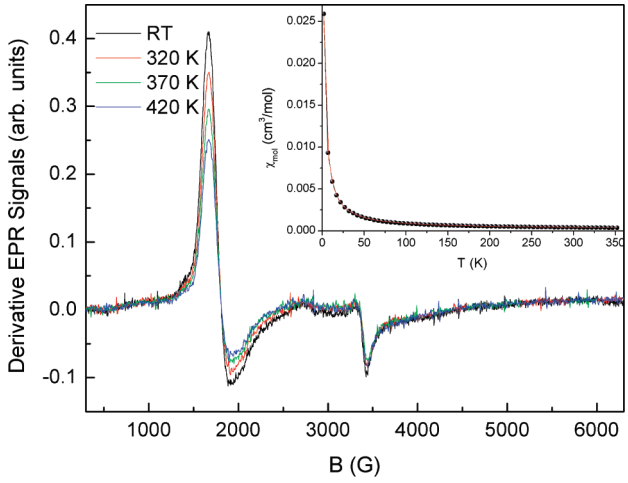

Figure 2. EPR spectrum of Cr050 in the temperature range of 300−420 K. In the inset, the magnetic susceptibility at 1000 Oe (black circles) is reported for the same sample together with the fit (red line) obtained with the Curie−Weiss law.

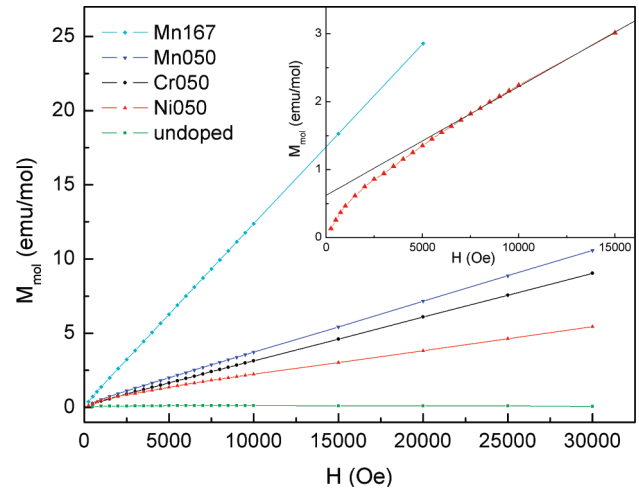

Figure 3. Molar magnetization vs H at 300 K for all the considered samples. The inset shows an enlarged view of the Ni050 curve compared to the linear fit of the highest field region of the same curve, extrapolated to $H = 0$.

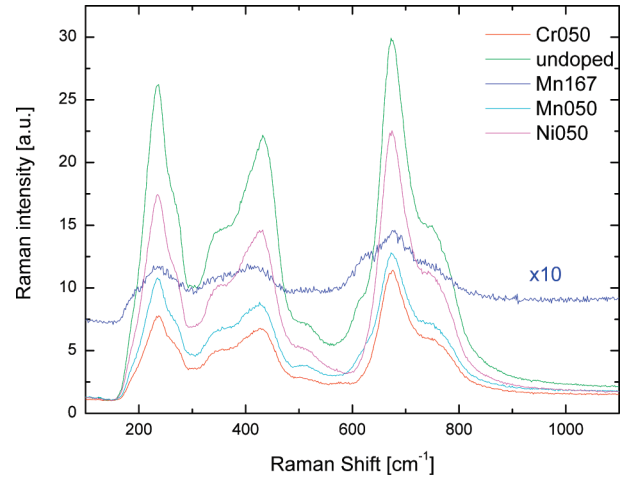

Figure 4. Raman spectra at room temperature of the undoped and doped powders.

in the case of a typical paramagnetic behavior (see Figure 2, showing the spectrum evolution in the temperature range of 300−420 K). No signal has been detected for the Ni-doped sample, for which the absence of any signal has been verified in the whole investigated temperature range (4−300 K). Both the spectra of Mn050 and Mn167, reported for comparison, show two signal components, centered at $g_{eff} \sim 4.3$ and $g_{eff} \sim 2$, which only differ in signal intensity according to the Mn amount in the sample. They have been attributed to Mn^{2+} ions, located in tetrahedral site.[23] The components at $g_{eff} \sim 4.3$ and $g_{eff} \sim 2$ are typically observed for Mn^{2+} ions in glass matrixes,[27] and their origin can be attributed to the presence of Mn^{2+} ions in different symmetry sites, i.e., with different E and D crystal field parameters values, greater or lower than hv, in the standard spin Hamiltonian. For this reason, in the following we will refer to this feature of the EPR signal, related to the spinel structural disorder induced by the doping,[23] as glassy character.

Finally, a weak sextet of hyperfine structure coming from the spin 5/2 Mn nucleus has been detected, overlapped to the broad line centered at $g_{eff} \sim 2$, only for the Mn050 sample, whereas no hyperfine splitting is revealed in the Mn167 spectrum.

3.3. Magnetization Results. For all the doped samples, the M versus T ($H = 1$ kOe) curves evidence an overall paramagnetic behavior, with no onset of long-range ordered magnetic phases. The magnetic susceptibility (χ) curves generally well obey to the Curie−Weiss law with negative values of the Weiss constant, indicating that antiferromagnetic-like local interactions occur between spins, consistently with dopant clustering, already supported by other experimental evidence in the case of Mn doping.[23] The χ curve for the Cr050 sample and the related fit are shown, as an example, in the inset of Figure 2. Actually, for the Ni050 sample some discrepancies from the Curie−Weiss curve have been detected. The peculiarity of Ni050, with respect to the other samples, is markedly evident in the M_{mol} versus H curves at r.t., reported in Figure 3. Although a nearly linear behavior is observed for all the other investigated samples, for Ni050 a not negligible deviation from linearity at low magnetic fields is revealed (see the inset of Figure 3), suggesting that Ni ions can also concur in giving rise to a short-range ferromagnetic-like behavior.

3.4. Micro-Raman. The micro-Raman spectra of the samples are shown in Figure 4. The Raman scattering features typical of the undoped $Li_4Ti_5O_{12}$[28] are well-evidenced in all samples. Each spectrum shows five main Raman bands peaked at about 237, 350, 432, 672, and 745 cm^{-1} representing the features of the spinel structure ($A_{1g} + E_g + 3F_{2u}$).[28] Differences can be observed comparing the intensities of Raman signals of the

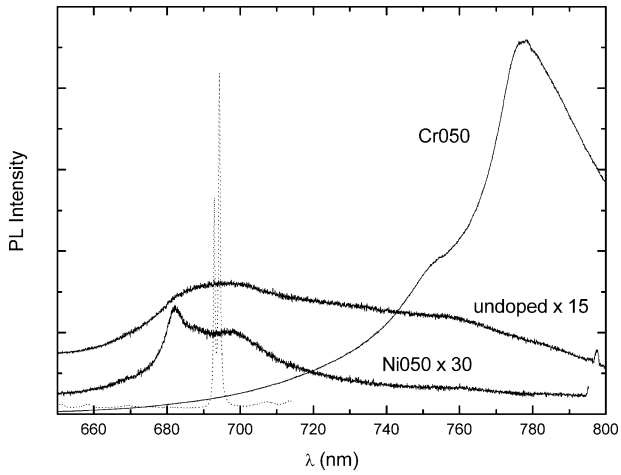

Figure 5. PL emission spectra obtained from undoped and Ni- and Cr-doped samples. The spectra of undoped and Ni-doped samples are multiplied by the factor indicated in the graph. As comparison, the dotted spectrum represents the PL emission (R-lines) of Cr^{3+} in the Al_2O_3 cage.

doped samples with that from the undoped compound. Indeed the Raman yield decreases markedly in doped with respect to the undoped ones. In addition, clearly appreciable is a broadening of all spectral features. Limiting the analysis to the most intense Raman signal at 675 cm^{-1}, i.e., the mode ascribable to Ti−O stretches in "TiO_6" octahedra, from the best-fitting procedure we obtain a line width of 48, 52, 56, and 65 cm^{-1} for the undoped, Ni-, Cr-, and Mn050-doped samples, respectively. For the Mn167 sample the low signal accompanied to a visible broadening of the band hinders a reliable estimation of the line width. The bands intensities and broadening decrease clearly indicate an increased disorder caused by doping, especially high in the case of Cr doping and for Mn samples.

Further indications come from photoluminescence (PL) excited by the blue light and reported in Figure 5. From the energy position of the peaks we can surely say that the PL signal comes from the Cr ions. We recall that 50 ppm of Cr^{3+} ions are enough to have strong PL signals in glasses.[29]

For instance, in undoped and Ni-doped samples there is the presence of broadened PL bands clearly associated to the typical Cr R-lines at around 690 nm (see the dotted spectrum in Figure 5). The broadening with respect to the case of Ruby emission indicates the presence of a certain degree of disorder, which in any case did not modify markedly the peak positions of the emission.

Differently, in the Cr-doped sample a marked red shift in the emission of Cr ions is observed, leading to an intense PL band centered at around 760 nm.

3.5. NMR. Figure 6 shows the ^7Li MAS spectra of the samples doped with chromium (Figure 6a) and nickel (Figure 6b). As a comparison, the spectrum of the undoped sample (Figure 6c), previously discussed,[23] is also shown. The spectra of Cr- and Ni-doped samples are characterized by a single line centered at 0 ppm and by a complex sideband manifold due to dipolar coupling among the Li nuclei and the unpaired electrons of Cr and Ni. Detailed analyses of the spin interactions in paramagnetic oxides were given in previous papers.[23,30] In both the cases, the dipolar coupling is partially removed by MAS rotation, and the residual magnetic interaction is stronger in the case of Cr050 than for the Ni050 sample. In fact, the former has a manifold width of more than 500 ppm (∼80 kHz) against less than 400 ppm (∼60 kHz) for the latter.

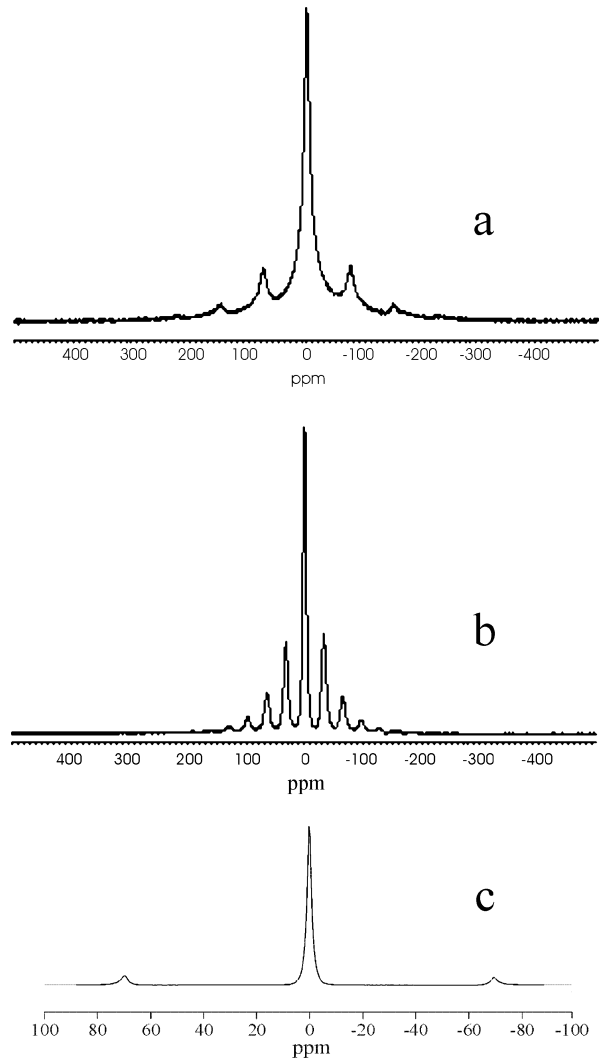

Figure 6. ^7Li MAS NMR spectra of Cr-doped (a), Ni-doped (b), and undoped (c) samples.

3.6. IS. Impedance spectroscopy data are used to evaluate the conductivity dependence on temperature for undoped, Ni050, Cr050, and Mn167 samples both in O_2 and N_2 flow. The Arrhenius plot is shown in Figure 7. In O_2 flow, the conductivity, all over the temperature range, decreases for Mn and Ni doping, whereas it slightly increases for Cr doping, if compared to that of the undoped sample. In N_2 flow, all the samples improve their conductivity with respect to the O_2 flow, especially the Mn- and Cr-doped ones.

4. Discussion

The structural refinement gives a clear indication that the insertion of the dopant ion in the spinel lattice really occurs in the case of the Cr doping: the lattice parameter value decreases after doping (Table 1), and changes in the MO_4 and MO_6 bond lengths (Table 1) with respect to those of undoped $Li_4Ti_5O_{12}$ (−0.55% and 0.25%, respectively) are obtained. The Raman spectrum suggests that, in spite of an appreciable line width increase, the average crystalline structure is maintained and the insertion of Cr did not change the main phonon vibrations.

The influence of Cr doping on the local $Li_4Ti_5O_{12}$ structural properties is also provided by the EPR line shape. According to our structural refinement, supported by neutron diffraction studies on Cr-doped $Li_4Ti_5O_{12}$,[13] the Cr insertion into the spinel lattice occurs in the octahedral 16d site so that it is reasonable

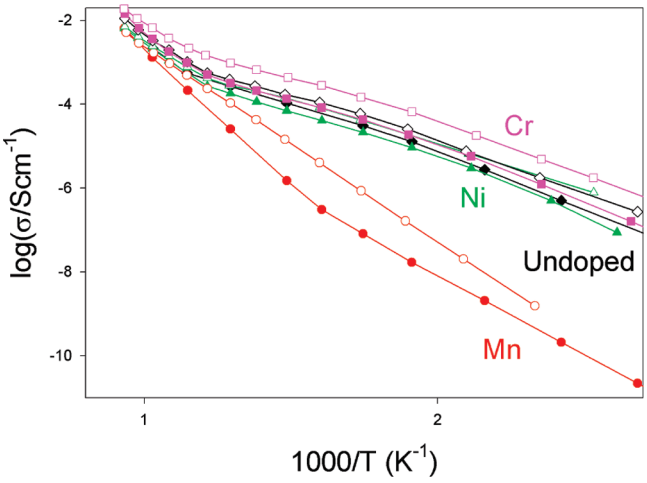

Figure 7. Arrhenius plot of conductivity data obtained in O_2 (closed symbols) and N_2 (open symbols) flow for undoped (diamond) and Cr050 (square), Ni050 (triangle up), and Mn167 (circle) samples.

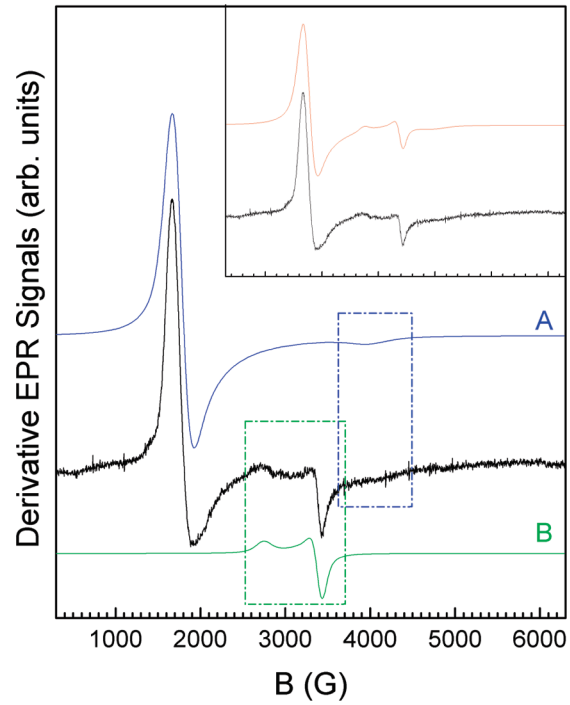

Figure 8. Room-temperature Cr050 EPR spectrum (black line) compared to the computed A and B components (see text). In the inset, the same spectrum is compared to the computed one obtained as sum of A and B components (red line).

to expect the Cr ion to have the +3 oxidation state, particularly stable in octahedral coordination[13,18,19] and also consistent with the use of Cr_2O_3 for the synthesis. For Cr^{3+} ions (d^3, $S = 3/2$) isotropic EPR signals centered at $g \sim 2$ are usually expected,[31] particularly in an octahedral crystal field of cubic symmetry,[32] as it should be in the case of the cubic $Li_4Ti_5O_{12}$ spinel. On the other hand, for the Cr050 sample the peculiar EPR spectrum consists in powder-like signals ($g_{eff} \sim 3.7$ and $g_{eff} \sim 2$) typically arising from axial g-tensor (Figures 1 and 2). We point out that the amount of the EPR centers giving rise to the Cr050 spectrum, estimated by comparing its area with that of a paramagnetic standard, is indeed consistent with the nominal Cr^{3+} amount in the sample. The Cr050 EPR line shape clearly indicates that the symmetry of Cr local environment considerably departs from the cubic one and, more generally, that the Cr substitution heavily affects the ordered and stable spinel structure. A similar behavior had been already observed in the case of Mn doping, which, in different amounts and after different synthesis procedures, unexpectedly induced structural disorder into the $Li_4Ti_5O_{12}$ matrix.[23] This was directly witnessed, in particular, by the glassy character of the EPR spectra, composed, for each sample, by the two signals centered at $g_{eff} \sim 4.3$ and $g_{eff} \sim 2$, as shown in Figure 1 for the two Mn-doped samples chosen as reference.

A signal computation by numerical methods has been performed to get more information on the local symmetry of the Cr^{3+} crystal sites. Figure 8 reports the experimental r.t. spectrum together with the best result obtained for the computed two main components (A and B in the figure). The signal resulting from the sum of A and B components is reported in the inset (red line), together with the experimental one (black line), for comparison. A and B come from two different Cr^{3+} centers, with axial symmetry due to distortions along a fourfold axis (here called the "z-axis") of the Cr^{3+} octahedral environment. Only octahedral Cr^{3+} centers have been considered for the signal deconvolution according to the Rietveld refinement results (Table 1).

Signal A, with $g_\perp > g_\parallel$ ($g_\perp \cong 3.9$, $g_\parallel \cong 1.7$), corresponding to a compression of the octahedron along the z-axis, reproduces, although not perfectly, the main signal component at $g_{eff} \sim 3.7$ and the one centered at about 4000 G (see the blue square in Figure 8). The paramagnetic character of the Cr^{3+} EPR signal around r.t., evidenced by the temperature dependence reported in Figure 2 and further confirmed by the overall paramagnetic character of the sample inferred from the magnetic susceptibility curve, excludes that the low-field component comes from local nonhomogeneous magnetic fields which would "move" the signal from the $g \cong 2$ position.

We try to explain the presence of this unexpected component at $g_{eff} \sim 3.7$ on the basis of the results obtained for Mn doping, for which a glassy behavior had been observed. We can hypothesize that this component, not perfectly reproducible with the computation method, is really due to the superposition of slightly different "A components", i.e., to octahedral Cr^{3+} centers with slightly different axial distortions. This could correspond to a continuous distribution of crystal field parameters values leading to a glasslike behavior, also compatible with the large ΔB value. In support of this, signals with $g_{eff} \sim 4$, and even higher, have been widely observed for Cr^{3+} ions in diamagnetic glassy matrixes; these signals are related to isolated octahedrally distorted sites subjected to strong crystal field effects (in agreement with the high L value ($L = 3$) of Cr^{3+} ions) giving rise to large zero-field splitting compared to the microwaves $h\nu$ value (refs 27, 33 and references therein, and 34). Especially, EPR signals with $g_x = g_y = 4$ and $g_z = 2$ values are theoretically foreseen for Cr^{3+} ions in sites subjected to strong crystal field effects, in the particular case of pure axial distortion of the Cr octahedral environment. In this case, in addition to the above axial signal, a component with $g_\parallel \cong 6$ (i.e., at about 1130 G, for our microwave's frequency, where we really observe a low-intensity resonance) and $g_\perp \cong 0$ is also foreseen, from forbidden transitions.[33] In the case of the $Li_4Ti_5O_{12}$ spinel, the distribution of axial distortions, due to the Cr doping, is consistent with the presence of sample regions with high Cr^{3+} concentration or, at least, to nonhomogeneous distribution of the dopant in the $Li_4Ti_5O_{12}$ structure.

The resonance at $g_{eff} \sim 2$ is usually expected for Cr^{3+} ions in crystal sites and is also commonly related, in glassy matrixes, to exchange-coupled Cr^{3+}–Cr^{3+} pairs[35] or, for low Cr concen-

tration, to isolated Cr^{3+} ions in weakly distorted sites.[36] In our case, the component centered at $g_{eff} \sim 2$ is well-reproduced by signal B, with $g_\perp < g_{||}$ ($g_\perp \cong 1.98$, $g_{||} \cong 2.47$), corresponding to a compression of the octahedron in the $x-y$ plane. A clearly lower degree of axial distortion with respect to the A case is deduced by the related Δg values. At the same time, a more limited distribution of distortions is inferred from the better simulation result for B with respect to the A component, possibly due to a better dilution in the $Li_4Ti_5O_{12}$ matrix of Cr^{3+} ions related to the B signal.

Some consideration can be made at this point: (i) the stoichiometric formula foresees that Ti and Li ions, respectively, occupy 5/6 and 1/6 of the undoped spinel octahedral sites; (ii) Li ions are well-diluted in the octahedral sites of the stoichiometric spinel structure; (iii) the signal areas ratio between the two observed main components is strongly favorable to the one at lower magnetic fields (~15:1); (iv) Cr^{3+}, Li^+, and Ti^{4+} have different ionic radii (r), in particular $r(Li^+) > r(Cr^{3+}) > r(Ti^{4+})$.[37]

The above observations seem to indicate that both Cr_{Ti} and Cr_{Li} substitutions occur in the octahedral sites, each of them giving rise to the A and B components, respectively, corresponding to opposite axial distortion of the relative octahedral environments. The Cr_{Li}-substituted octahedral sites are better diluted, according to the cation distribution in the spinel structure, whereas the more glassy character and the higher intensity of the EPR signal related to the Cr_{Ti}-substituted octahedral sites indeed support the hypothesis of clustering or nonhomogeneous Cr distribution. This is also consistent with the NMR results. In fact, in contrast to what was observed in the case of Mn-doped spinels,[23] we have not evidence of Fermi-contact (FC) or pseudocontact (PC) shifts either for Cr050 or Ni050, whose spectra seem instead to be both originated by through-space delocalized magnetic interactions. Although we cannot fully rule out that the absence of FC or PC contributions is simply due to relatively low Cr and Ni substitution levels, our results call for cations clustering or, at least, nonhomogeneous distributions of the dopants on the octahedral spinel sites. On the other hand, we cannot also exclude that a part of ^7Li nuclei close to the Ni or Cr "clusters" are broadened beyond observation.

A further confirmation of this reasoning can be inferred by the PL shape and peak position observed in Cr050 samples. The observed red shift is a clear indication that the energy levels and the transitions rules are markedly affected by a high degree of disorder. Similar Cr^{3+} emission has been observed in glasses, and this supports the idea that the Cr doping causes in $Li_4Ti_5O_{12}$ a marked decrease of crystalline order with a behavior similar to a glassy system.

For the Cr050 sample, the conductivity in O_2 flow slightly increases with respect to that of the undoped sample in the whole temperature range. This is in agreement with literature results on samples with higher Cr content,[18] and with theoretical ones,[24] and suggests a slight increase of electronic conductivity by Cr doping: the Cr 3d bands are close to the Ti 3d ones, and the hopping transport of the 3d electrons via the Cr and Ti ions is feasible. The increase in conductivity in N_2 flow, shown also by the undoped sample, suggests the presence of oxygen vacancies as intrinsic defect, because no impurities have been detected and the stoichiometry in the cationic framework reported in Table 1 is charge-balanced and coincides with the synthesis composition.

Concerning the Ni doping, the Rietveld refinement (Table 1) suggests that Ni is located exclusively on the octahedral spinel site. The refined lattice parameter and tetrahedral and octahedral bond lengths are practically unchanged with respect to those obtained for the undoped sample. These evidence could be explained by the very close values of the Ti^{4+} and Ni^{3+} ionic radii (0.605 and 0.600 Å, respectively[37]) and/or by the fact that a not complete substitution of the Ni ions into the cationic framework occurs. In addition the line width broadening of Raman band at 672 cm^{-1} with respect to the undoped sample is appreciable but lower than that observed for Cr sample, indicating a less degree of disorder. This fact results also from the PL signal of Cr traces, with the energies of the peaks slightly different from that observed in Ruby.

The absence of any EPR signals prevents us to get reliable information on the Ni valence state and on its local environment. Notwithstanding, on the basis of the Mn and Cr influence on the spinel matrix, it is fair to foresee that the formation of clusters or nonhomogeneous distribution on the octahedral spinel sites can occur also for the Ni substitution, as anyway suggested by the NMR results. The nonhomogeneous Ni distribution and even more the presence of regions with high concentration of Ni ions, which, like in the case of Mn and Cr ions, would occupy sites characterized by different local distortions, can really induce a broadening of the EPR line width with no detection of the signal, similarly to what is already observed in the case of polycrystalline compounds with the capability to host transition cations in a glasslike matrix.[38] At our measuring frequency (X-band) the lack of EPR signal, especially from Ni^{2+} ions, could also partially be consequence of crystal field effects leading to zero-field splitting of the energy levels. The presence of Ni clustering is consistent with the not negligible ferromagnetic-like contribution to M, observed already at r.t. (see Figure 3 and inset). We point out that no long-range order is evident from the χ_{mol} curve and, in addition, no Ni-containing ferromagnetic-like phase is indeed evidenced from XRPD patterns.

The slight decrease of conductivity observed in the Ni050 sample with respect to the undoped one is in agreement with the theoretical findings:[24] the electronic conductivity of $Li_4Ti_5O_{12}$ at low Ni doping level cannot be improved, because Ni 3d bands are localized and electrons are not easily excited. The conductivity in N_2 flow (Figure 7) shows an increase with respect to the data obtained in O_2 flow, suggesting the presence of oxygen vacancies, as for the undoped and Cr-doped sample.

The ions distribution in the cationic framework can help in explaining the conductivity behavior both in O_2 and in N_2 flow. In the case of Ni doping, TiO_2 and Li_2TiO_3 impurity phases are detected by XRPD and Ni ions are completely located on the octahedral site. The following formula can be estimated on the basis of the calculated stoichiometry (Table 1), depending on the possible oxidation state n of Ni ions ($n = +2$ or $+3$): $[Li^+_{1.000}]_T[Li^+_{0.279}Ni^n_{0.053}Ti^{4+}_{1.668}]_O$. An excess of positive charges is evaluated in the cationic framework, independently of the Ni oxidation state. The charge balancing can be reached by reduction of Ti^{4+} to Ti^{3+} or by cation vacancies formation. The first hypothesis should be excluded due to the absence of Ti^{3+} EPR signal. Instead, the poor X-ray scattering power of Li ions does not allow us to exclude the Li^+ vacancies formation. Ni^{2+} or Ni^{3+} vacancies could also be taken into consideration, if not all the Ni ions inserts into the $Li_4Ti_5O_{12}$ cationic framework, as suggested by the refinement of the lattice parameter, unchanged with respect to the value obtained for the undoped sample. Moreover, the presence of traces of NiO impurity phase, antiferromagnetic in the whole EPR and magnetic susceptibility investigated temperature range, cannot be excluded. Besides, the presence of the not negligible ferromagnetic-like contribution to M, and so the possibility of the Ni clustering, suggests that

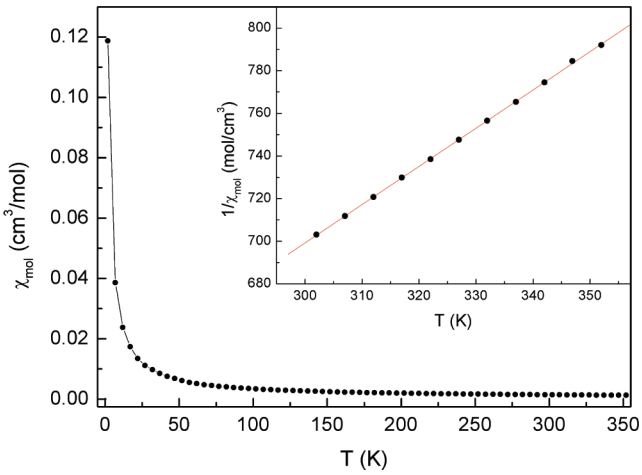

Figure 9. χ_{mol} vs T at 1 kOe for Mn167. Inset: $1/\chi_{mol}$ curve for $T >$ 300 K for the same sample along with the linear fit (red line).

the fraction of Ni ions that really play the role of dopant in $Li_4Ti_5O_{12}$ may be lower than 0.053, deduced by the previous calculation.

The effect of Mn doping on the $Li_4Ti_5O_{12}$ compound has been deeply discussed.[23] Anyway, additional considerations come out of the magnetization and Raman results. The weakening of the Raman yield, especially in Mn167, and the broadening of the main Raman bands, support the fact that Mn doping causes a high degree of disorder probably associated to clusterization processes, even if, for instance, no clear signatures of Raman modes from Mn oxides have been evidenced.

Concerning the magnetic behavior, we have already pointed out here that, although no onset of long-range order is evidenced, the negative Weiss temperature suggests that antiferromagnetic-like local interactions occur between Mn ions, consistently with the formation of Mn clustering, also supported by the very low intensity and/or absence of the resolved hyperfine structure in the EPR spectra.[23] Besides, the average effective number of Bohr magnetons for the Mn ion resulting from the slope of the $1/\chi_{mol}$ curve in the high-temperature region is in good agreement with the compositional model obtained by means of other techniques[23] and reported in Table 1. Figure 9 evidences the overall paramagnetic behavior of the molar magnetic susceptibility curve for Mn167, while the linear trend of the $1/\chi_{mol}$ curve in the high-temperature range is shown in the inset.

For the Mn doping, the conductivity in N_2 flow (Figure 7) is significantly increased with respect to that in O_2 flow, suggesting the formation of oxygen vacancies, additional to the intrinsic ones, to balance the lack of the positive charges on the cationic framework of the spinel structure. In fact, the charge distribution $[Li^+_{0.985}Mn^{2+}_{0.002}Mn^{3+}_{0.013}]_T[Li^+_{0.348}Mn^{3+}_{0.036}Ti^{4+}_{1.616}]_O$ for Mn050 and $[Li^+_{0.963}Mn^{2+}_{0.024}Mn^{3+}_{0.013}]_T[Li^+_{0.313}Mn^{3+}_{0.144}Ti^{4+}_{1.543}]_O$ for the Mn167 sample can be obtained by combining the refined Mn distribution reported in Table 1 and the valence state of the doping ion, determined by a multitechnique approach:[23] the Mn^{3+} occupies the octahedral site (O), while a fixed amount of Mn^{3+} (0.013) and all the Mn^{2+} are on the tetrahedral one (T).

On the basis of the previous discussion on cation distribution and valence state, impurity phases amount, local/average order, and clustering for Cr, Ni, and Mn doping ions in the $Li_4Ti_5O_{12}$ matrix, we can now outline the peculiar influence of each doping ion on the functional properties, in particular on the electrical behavior, of the investigated compound. Undoped and Ni- and Cr-doped samples show practically the same conductivity trend (Figure 7) in O_2 flow. For the same samples, a possible creation of oxygen vacancies, by annealing in N_2 flow, causes the most evident increase in conductivity in the Cr sample, indicating the pertinent electrons concentration increase. A similar behavior was observed in the Mn-doped sample (Figure 7), whose conductivity level is more than 3 orders of magnitude lower, in the temperature range of 300−600 K. These lower conductivity data of the Mn-doped sample are in agreement with the different distribution of Mn ions (on both crystallographic sites) with respect to the Cr- and Ni-doped samples, in which the transition cations are found on the octahedral site only. In the Ni-doped sample, the charge balance may be obtained through a small cation vacancy fraction (V_{Li}), whose presence may justify the slightly lower conductivity values in the whole temperature range and also the very little increase in conductivity after changing atmosphere from O_2 to N_2 flow.

5. Conclusions

The combined use of different structural and spectroscopic techniques allowed us to get new information on the local and average structural features of the Cr- and Ni-doped $Li_4Ti_5O_{12}$. XRPD data suggest that both doping ions are located on the octahedral site of the spinel cubic lattice. The Cr substitution strongly affects the cubic spinel structure, similarly to the Mn addition,[23] leading to a glasslike behavior at least as far as concerns the EPR features. The Cr^{3+} substitution of Ti^{4+} and Li^+ ions, located on the same crystallographic site, gives rise to opposite axial distortion of the relative octahedral environments. The glassy character of the EPR spectrum is consistent with the dopant clustering evidenced by ^{7}Li NMR-MAS and micro-Raman results. A clustering phenomenon is also foreseen in the case of Ni doping, further supported by magnetization data. The IS measurements indicate that, among the investigated doping ions, only Cr leads to an increase of conductivity with respect to the undoped sample. Possible defect models concerning oxygen or cation vacancies are proposed to obtain the proper charge balance and to explain the conductivity behavior of the samples.

Acknowledgment. A partial funding by the CARIPLO Foundation (Project "Nuove membrane elettrolitiche nanocomposite a base di liquidi ionici" 2006) is gratefully recognized.

References and Notes

(1) Goodenough, J. B.; Manthiram, A.; Wnetrzewski, B. *J. Power Sources* **1993**, *43*−*44*, 269.
(2) Koksbang, R.; Barker, J.; Shi, H.; Saidi, M. Y. *Solid State Ionics* **1996**, *84*, 1.
(3) Scharner, S.; Weppner, W.; Schmid-Beurmann, P. *J. Electrochem. Soc.* **1999**, *146*, 857.
(4) Jansen, A. N.; Kahaian, A. J.; Kepler, K. D.; Nelson, P. A.; Amine, K.; Dees, D. W.; Vissers, D. R.; Thackeray, M. M. *J. Power Sources* **1999**, *81*−*82*, 902.
(5) Chen, C. H.; Vaughey, J. T.; Jansen, A. N.; Dees, D. W.; Kahaian, A. J.; Goacher, T.; Thackeray, M. M. *J. Electrochem. Soc.* **2001**, *148*, A102.
(6) Bach, S.; Pereira-Ramos, J. P.; Baffier, N. *J. Mater. Chem.* **1998**, *8*, 251.
(7) Hao, Y.; Lai, Q.; Liu, D.; Xu, Z.; Ji, X. *Mater. Chem. Phys.* **2005**, *94*, 382.
(8) Hao, Y.; Lai, Q.; Xu, Z.; Liu, D.; Ji, X. *Solid State Ionics* **2005**, *176*, 1201.
(9) Venkateswarlu, M.; Chen, C. H.; Do, J. S.; Lin, C. W.; Chou, T. C.; Hwang, B. J. *J. Power Sources* **1995**, *146*, 204.
(10) Hao, Y.; Lai, Q.; Lu, J.; Wang, H.; Chen, Y.; Ji, X. *J. Power Sources* **2006**, *158*, 1358.
(11) Rho, J. H.; Kanamura, K.; Umegaki, T. *Chem. Lett.* **2001**, *30*, 1322.
(12) Ganesan, M. *Ionics* **2008**, *14*, 395.
(13) Robertson, A. D.; Trevino, L.; Turamoto, H.; Irvine, J. T. S. *J. Power Sources* **1999**, *81*−*82*, 352.
(14) Robertson, A. D.; Turamoto, H.; Irvine, J. T. S. *J. Electrochem. Soc.* **1999**, *146*, 3958.

(15) Scharner, S.; Weppner, W.; Schmid-Beurmann, P. *J. Solid State Chem.* **1997**, *134*, 170.
(16) Reale, P.; Panero, S.; Ronci, F.; Rossi Albertini, V.; Scrosati, B. *Chem. Mater.* **2003**, *15*, 3437.
(17) Jovic, N.; Antic, B.; Kremenovic, A.; Spasojevic-de Bire, A.; Spasojevic, V. *Phys. Status Solidi A* **2003**, *198*, 18.
(18) Nakayama, M.; Ishida, Y.; Ikuta, H.; Wakihara, M. *Solid State Ionics* **1999**, *177*, 265.
(19) Ohzuku, T.; Tatsumi, K.; Matoba, N.; Sawai, K. *J. Electrochem. Soc.* **2000**, *147*, 3592.
(20) Huang, S.; Wen, Z.; Zhu, X.; Lin, Z. *J. Electrochem. Soc.* **2005**, *152*, A186.
(21) Hernandez, V. S.; Torres Martinez, L. M.; Mather, G. C.; West, A. R. *J. Mater. Chem.* **1996**, *6*, 1533.
(22) Leonidov, I. A.; Leonidova, O. N.; Samigullina, R. F.; Patrakeev, M. V. *J. Struct. Chem.* **2004**, *45*, 262.
(23) Capsoni, D.; Bini, M.; Massarotti, V.; Mustarelli, P.; Chiodelli, G.; Azzoni, C. B.; Mozzati, M. C.; Linati, L.; Ferrari, S. *Chem. Mater.* **2008**, *20*, 4291.
(24) Liu, D.; Ouyang, C.; Shu, J.; Jiang, J.; Wang, Z.; Chen, L. *Phys. Status Solidi B* **2006**, *243*, 1835.
(25) Bruker AXS. *TOPAS V3.0: General Profile and Structural Analysis Software for Powder Diffraction Data*; User Manual Bruker AXS: Karlsruhe, Germany, 2005.
(26) Chiodelli, G.; Lupotto, P. *J. Electrochem. Soc.* **1991**, *9*, 2703.
(27) Griscom, D. L. *J. Non-Cryst. Solids* **1980**, *40*, 211.
(28) Aldon, L.; Kubiak, P.; Womes, M.; Jumas, J. C.; Olivier-Fourcade, J.; Tirado, J. L.; Corredor, J. I.; Perez Vicente, C. *Chem. Mater.* **2004**, *16*, 5721.
(29) Han, T. P. J.; Jaque, F.; Jaque, D.; Ivleva, L. *Chem. Phys. Lett.* **2006**, *417*, 196.
(30) Mustarelli, P.; Massarotti, V.; Bini, M.; Capsoni, D. *Phys. Rev. B* **1997**, *55*, 12018.
(31) Massarotti, V.; Capsoni, D.; Bini, M.; Azzoni, C. B.; Mozzati, M. C.; Galinetto, P.; Chiodelli, G. *J. Phys. Chem. B* **2006**, *110*, 17798.
(32) Abragam, A.; Bleaney, B. *Electron Paramagnetic Resonance of Transition Ions*; Clarendon Press: Oxford, 1970; pp 430−434.
(33) Ardelean, I.; Peteanu, M.; Simon, V.; Bob, C. *J. Mater. Sci.* **1998**, *33*, 357.
(34) Haouari, M.; Ben Ouada, H.; Maaref, H.; Hommel, H.; Legrand, A. P. *J.Phys.: Condens. Matter* **1997**, *9*, 6711.
(35) Landry, R. J.; Fournier, J. T.; Young, C. G. *J. Chem. Phys.* **1967**, *46*, 1285.
(36) Legein, C.; Buzaré, J. Y.; Emery, J.; Jacoboni, C. *J. Phys.: Condens. Matter* **1995**, *7*, 3853.
(37) Shannon, R. D. *Acta Crystallogr.* **1976**, *A32*, 751.
(38) Massarotti, V.; Capsoni, D.; Bini, M.; Azzoni, C. B.; Mozzati, M. C.; Galinetto, P. *J. Phys. Chem. C* **2007**, *111*, 6857.

JP906894V